JOURNAL OF SYNCHROTRON RADIATION
ISSN 1600-5775

Track analysis of a synchrotron X-ray photoelectric nanoradiator by *in situ* fluorescence imaging of reactive oxygen species: comparative study of gold and iron oxide nanoparticles

Jae-Kun Jeon and Jong-Ki Kim*

Department of Biomedical Engineering, School of Medicine, Catholic University of Daegu, Daegu 42472, Republic of Korea. *Correspondence e-mail: jkkim@cu.ac.kr

Received 27 April 2018
Accepted 9 August 2018

Edited by I. Lindau, SLAC/Stanford University, USA

Keywords: X-ray photoelectric nanoradiator; ROS-oxidant fluorescence; gel dosimetry; track analysis; gold nanoparticles; iron oxide nanoparticle.

The emission of fluorescent X-rays and low-energy electrons by mid-/high-Z nanoparticles upon irradiation with either X-ray photons or high-energy ion beams is referred to as the nanoradiator effect (NRE). A track analysis of NRE was performed using reactive oxygen species (ROS) gels, to which macrophages containing gold nanoparticles (AuNPs) were attached, together with single-cell irradiation of the intracellular nanoparticles from a microbeam of synchrotron X-rays, and the range and distribution of $^{\bullet}OH$ and $O_2^{\bullet-}$ produced were compared with those of the Fe-nanoradiator by magnetite nanoparticles (FeONP, Fe_3O_4). The Au-nanoradiator generated ROS fluorescence to a greater depth and wider angle with respect to the incident X-rays than that of the Fe-nanoradiator. The ROS-oxidant fluorescence intensity ratios of $^{\bullet}OH$ to $O_2^{\bullet-}$ were different for the AuNPs and FeONPs, reflecting different relative yields of electrons and fluorescent X-rays from NRE. In the region immediately (<100 µm) below the irradiated cell, $^{\bullet}OH$-radicals were distributed mainly along two or three tracks in the depth direction in the FeONP- or AuNP-ROS gel. In contrast, $O_2^{\bullet-}$ was scattered more abundantly in random directions in the AuNP-ROS gel than in the FeONP-ROS gel. Track analysis of X-ray photoelectric nanoradiator radiation showed a different range of dose distribution and relative emission compositions between Au- and Fe-nanoradiators, suggesting more extensive damage beyond a single cell containing AuNPs than one containing FeONPs.

1. Introduction

The irradiation of mid-/high-Z nanoparticles with X-ray photons (Carter *et al.*, 2007; Haume *et al.*, 2016), gamma radiation (Wolfe *et al.*, 2015; Schuemann *et al.*, 2016) or high-energy charged particles (Kim *et al.*, 2010: Porcel *et al.*, 2014) ionizes atoms in the nanoparticles, followed by burst emissions of low-energy electrons and fluorescent X-ray photons through an Auger cascade process on the directly ionized atoms and an interatomic de-excitation path to adjacent neutral atoms (Kim *et al.*, 2012; Gokhberg *et al.*, 2014; Seo *et al.*, 2015). When this nanoprocess, termed the nanoradiator effect (NRE), occurs in a target tissue, the NRE alone can produce a therapeutic effect (Jeon *et al.*, 2016*a*; Kim *et al.*, 2012), or the NRE-mediated dose enhancement can increase the therapeutic efficiency of radiation therapy (Hainfeld *et al.*, 2008; Yang *et al.*, 2018). Gold and magnetite nanoparticles have shown comparable therapeutic enhancements in animal disease models by the induction of NRE *via* proton-induced Coulomb interactions or X-ray photoelectric absorption despite their difference in Z number (Kim *et al.*, 2012; Jeon *et al.*, 2016*a*; Choi *et al.*, 2012). A comparative study of NRE was

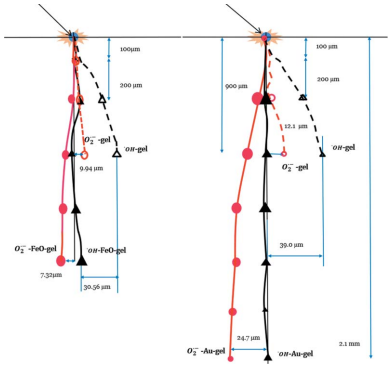

recently performed by quantitative measurements of ROS production by proton-irradiated AuNPs and FeONPs (Seo *et al.*, 2017). The range of NRE-mediated radiation transport to the surrounding medium as well as the resulting tissue damage can be important factors in NRE-enhanced therapy that may be determined by track analysis of the NRE-dose distribution.

Delivering gold or iron oxide nanoparticles to the inflammatory target site often requires intravenous injection of the nanoparticles, where they are encapsulated by plasma macrophages and then transported to the target site while nanoparticles are taken up again by tissue macrophages such as TAM (Penn *et al.*, 2018; Vinogradov *et al.*, 2014). Therefore, macrophage-given nanoparticles often become the therapeutic target.

A prior study (Jeon *et al.*, 2016*b*) established the track analysis of FeONP-mediated NRE by using a macrophage cell-attached three-dimensional (3D) ROS gel, and found an extended range of energy transfer from NRE radiation to ROS production compared with that of incident X-rays alone. In this study, a single macrophage cell containing gold nanoparticles (AuNPs) was activated by a microbeam of polychromatic synchrotron X-rays to induce AuNP-mediated NRE. The track analysis of the Au-nanoradiator was performed by confocal laser-scanning microscopy along the depth of propagation of the radiation and was then compared with previous results obtained for an Fe-nanoradiator.

2. Methods and materials

2.1. 3D ROS gels

Gels containing fluorescent probes, here termed ROS gels, were prepared by using agarose gel in a 1 ml tube embedded in rubber clay as described previously (Jeon *et al.*, 2016*b*). Briefly, agarose solutions (0.2%) containing either 5 m*M* 2-[6-(4′-amino) phenoxy-3*H*-xanthen-3-on-9-yl] benzoic acid (APF) or 100 m*M* hydroethidine-dihydroethidium (DHE) solution were magnetically stirred at 40°C in a nitrogen environment for homogeneous mixing prior to gel formation. Macrophages containing AuNPs were incubated with the culture medium on the surface of the agarose gel coated with poly-L-lysine for cell growth. The gel (APF-AuNP gel or DHE-AuNP gel) was mounted on the sample holder. Similar cell-coated gel phantoms (*i.e.* without nanoparticles; APF gel, DHE gel) were prepared for the control experiments.

2.2. Intracellular nanoparticle concentration

The cellular uptake of gold nanoparticles was measured using an inductively coupled plasma (ICP-MS) mass spectrometer (Thermo Jarrell Ash ARISAP, USA) after incubation with 1 mg ml^{-1} AuNP. A total of 2.5 × 10^6 macrophage cells were plated in a Petri dish containing the nanoparticle solution. The measured data were presented as the average uptake density (μg Au per 10^6 cells) after harvesting the cells for the ICP-MS measurements.

Table 1
Intracellular concentration of nanoparticles in macrophages.

Cell number (×10^6)	Incubation (mg mL^{-1})	Uptake density (μg per 10^6 cells)		NP number (per cell)†
3.0	1.0	6.53	Fe	∼10^6
2.5	1.0	1.48	Au	∼65000

† Approximated estimation. In the unit volume of a cell, uptake density presents ∼1.6 × 10^{-3} μg Au per μm^3.

2.3. Photoelectric nanoradiator

The X-ray irradiation of a selected cell containing AuNPs was carried out *in vacuo* using synchrotron radiation at the PAL 4B bending-magnet beamline. The entire area of the selected cell was probed using a scanning polychromatic (5–14 keV; 5 keV as the lowest photon energy and 14 keV as the highest) microbeam with a diameter of 5 μm. Since the typical size of the macrophage cell was estimated to be 10 mm, the X-ray beam scanned four times to cover the entire area of the cell. The radiation dose was measured with a UNIDOSE dosimeter using a Farmer-type chamber, and the total exposure was 3 s at a dose rate of 240 mGy s^{-1}. A selected cell in each ROS gel phantom (APF-AuNP gel, APF gel, DHE-AuNP gel, DHE gel) was irradiated at the same position in the sample holder to ensure an identical environment of primary incident X-rays.

2.4. Confocal laser scanning microscopy

The irradiated agarose ROS gel was sectioned into 200 μm-thick samples using a microtome (Micro Slicer, DTK-2000, DSK). The sections were mounted on microscopy slides, and the fluorescence of either APF (λ_{em} = 532 nm) or DHE (λ_{em} = 635 nm) was examined under a confocal laser-scanning fluorescence microscope (Nikon, A1). The fluorescence intensity was analyzed using the default software of the confocal microscope, and its track was plotted using *Amira* software (VSG Inc., Burlington, USA) for image processing.

3. Results and discussion

The average concentration of AuNPs taken up by a macrophage cell was comparable with the cellular uptake of ions, despite the different number density as summarized in Table 1. Alginate-coated FeONPs and citrate-coated AuNPs are similar in size (13–15 nm), but resulted in different cellular uptake owing to the cellular specificity of the surface coatings (Cho *et al.*, 2010; Nambara *et al.*, 2016). However, the number density of AuNPs per cell was on a similar scale with other results (Xie *et al.*, 2017; Rothen-Rutishauser *et al.*, 2013). The ROS-oxidant fluorescence of APF and DHE resulting from $^{\bullet}$OH and $O_2^{\bullet-}$, respectively, represented their derivation from either primary incident X-rays or nanoradiator-mediated fluorescent X-rays (X-FL) and low-energy electrons, as shown in Fig. 1 (Seo *et al.*, 2017). ROS-fluorescence imaging of the gel showed the nanoradiator track from a typical cytoplasmic distribution of AuNPs in a selected cell under irradiation with

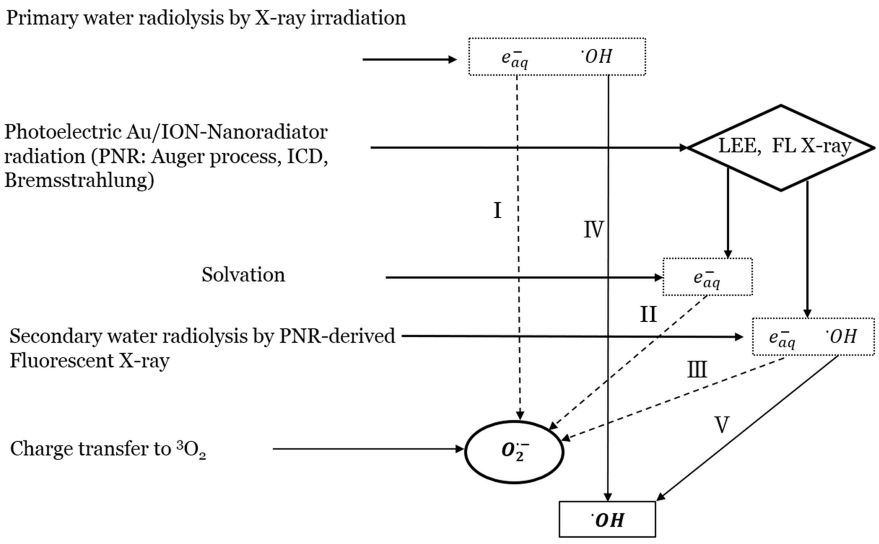

Figure 1
Schematic diagram of ROS production by water radiolysis after the nonhomogeneous chemical stage (10^{-12}–10^{-6} s) in the presence of proton-irradiated mid-/high-Z NPs at the time of detection with fluorescent probes. Energy transfer paths *via* IV and V indicate derivation of hydroxyl radicals from primary X-rays and fluorescent photoelectric nanoradiator (PNR)-mediated X-rays, whereas the others show generation of superoxide radicals from PNR-mediated low-energy electrons (II) and radiolysis by X-rays (I, III).

an X-ray microbeam. In the area immediately (<100 µm) beneath the cell-attached gel surface, three major tracks of APF-fluorescence appeared in the ROS-FeONP gel, whereas two tracks were observed in the ROS-AuNP gel, as shown in Fig. 2. The central track may be overlapped with the incident X-rays, and the other tracks are presumably a result of nanoradiator X-FL. Three subsets of Au L-lines (~13 K eV) were detectable from the Au-nanoradiator, wheras Fe K-lines (~7 K eV) were detectable from the Fe-nanoradiator, as previously observed by PIXE measurements from proton-irradiated FeONPs or AuNPs (Kim *et al.*, 2010). In contrast, $O_2^{\bullet-}$ derived DHE-fluorescence from electrons, resulting from either primary water radiolysis or the nanoradiator, were scattered through the ROS gel within a depth of 100 µm. The plotted areas of ROS-oxidant fluorescence from the ROS-AuNP gel were

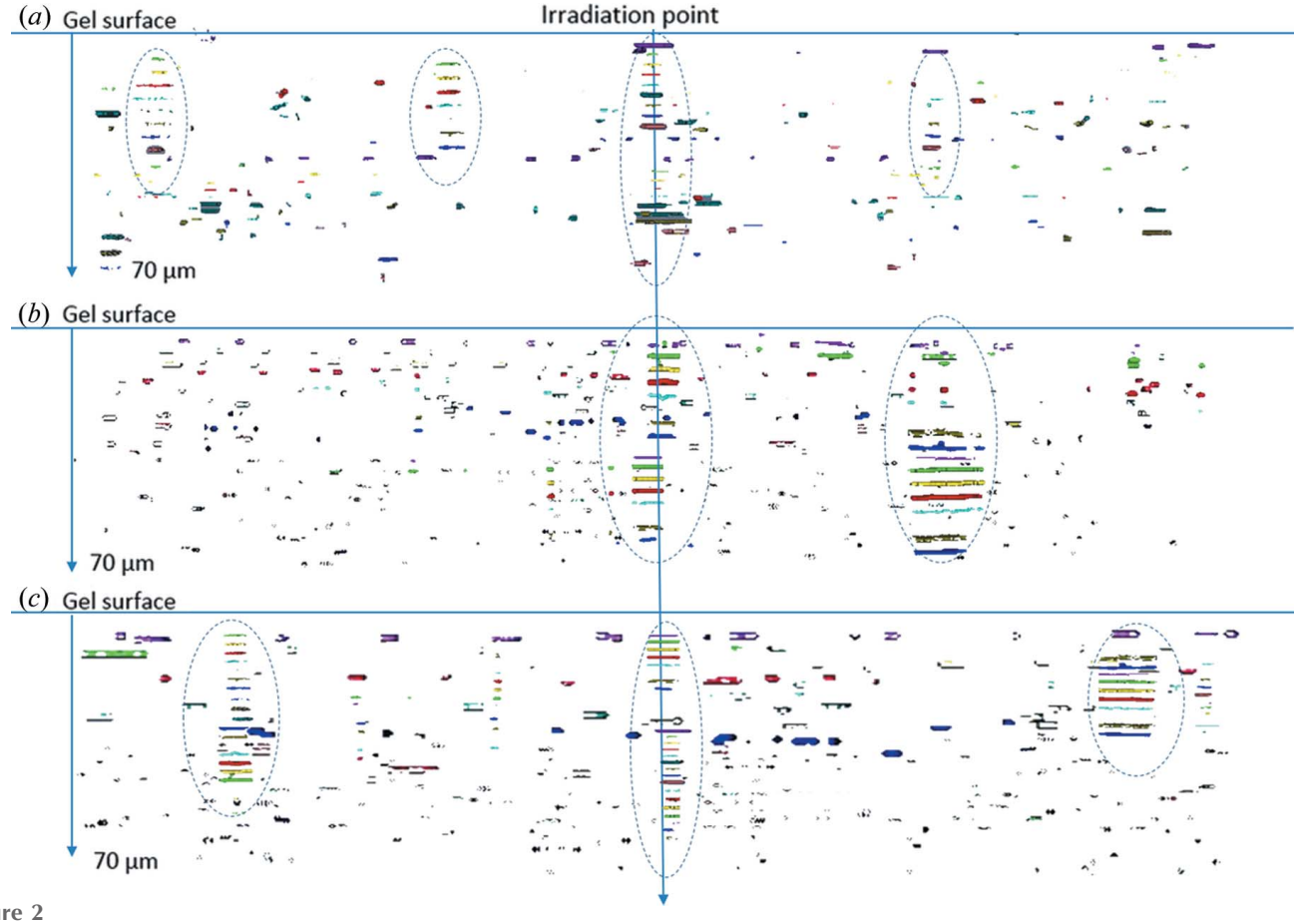

Figure 2
ROS distribution from either X-ray or electron emission in the region beneath the gel surface where cells were attached. ROS detected by APF gel or DHE gel under X-ray irradiation in the (*a*) absence or (*b*) presence of FeONPs and (*c*) AuNPs. Incident X-rays or nanoradiator X-FL generated a central or deflected track, while electrons produced by primary radiolysis or the nanoradiator were scattered in random directions. (*c*) Three tracks or (*b*) two tracks were observed for Au L-line X-FL or Fe K-line X-FL.

larger than those of the ROS gel without nanoparticles (see Fig. 2), indicating nanoradiator-mediated enhancement of the production of hydroxyl radicals or superoxide during the passage of propagation. These results are consistent with the dose enhancement by large-Z nanoparticles irradiated with X-rays shown in previous reports (Choi *et al.*, 2012; Carter *et al.*, 2007; Hainfeld *et al.*, 2008; Leung *et al.*, 2011; Lechtman *et al.*, 2011). However, the difference between the ROS-AuNP gel and ROS-FeONP gel in this study lay not only in dose enhancement but also in differential uptake density of the nanoparticles into cells. Interestingly, beyond 100 µm, multiple areas of ROS-oxidant fluorescence were converted into single-spot fluorescence in both the ROS-AuNP gel and the ROS-FeONP gel, as shown in Fig. 3. ROS tracks, resulting from the Au-nanoradiator, were observed continuously to a depth of 2.1 mm, which was greater than either the depths of 0.9 mm for the incident X-rays or 1.5 mm for the Fe-nanoradiator. These results indicated a potential role of nanoradiators as a new radiation source, acting as an internal emitter at the nanoparticle site. Moreover, the multiple-oxidant fluorescence (only within 100 µm) indicated limited penetration of the nanoradiator-induced electrons from the site of generation because of their low energy, typically less than several hundred electron volts, attributed to Auger electrons (Pradhan *et al.*, 2009) or inter-atomic Coulomb decay-type electrons (Gokhberg *et al.*, 2014). In contrast, X-FL derived from the nanoradiator penetrated to a much greater depth. The difference in penetration between the Au-nanoradiator and Fe-nanoradiator was attributed to differences in the X-ray energy of the characteristic X-FL from AuNPs (13 keV) and FeONPs (7 keV). Because X-FL may interact directly with cellular components or induce water radiolysis while producing $O_2^{\bullet-}$ and $^{\bullet}OH$ within a short attenuation length, it is effectively able to generate high linear energy transfer (LET) radiation and damage cells in a highly localized manner. These interpretations were evident from the observation of parallel distribution of the fluorescent ROS track by $O_2^{\bullet-}$-DHE and $^{\bullet}OH$-APF, as shown in Fig. 3. In addition, the $O_2^{\bullet-}$ track from the Au-nanoradiator showed larger angular deflection with respect to the $^{\bullet}OH$ track from incident X-rays than that from the Fe-nanoradiator, suggesting a wider overall effect of the Au-nanoradiator in irradiated tissues. Taken together, the ROS tracks reaching a depth of 1.5–2.1 mm suggested that the tissue damage caused by nanoradiators in cells can extend beyond the dimensions of a single cell, and the Au-nanoradiator produces more extensive damaging effects.

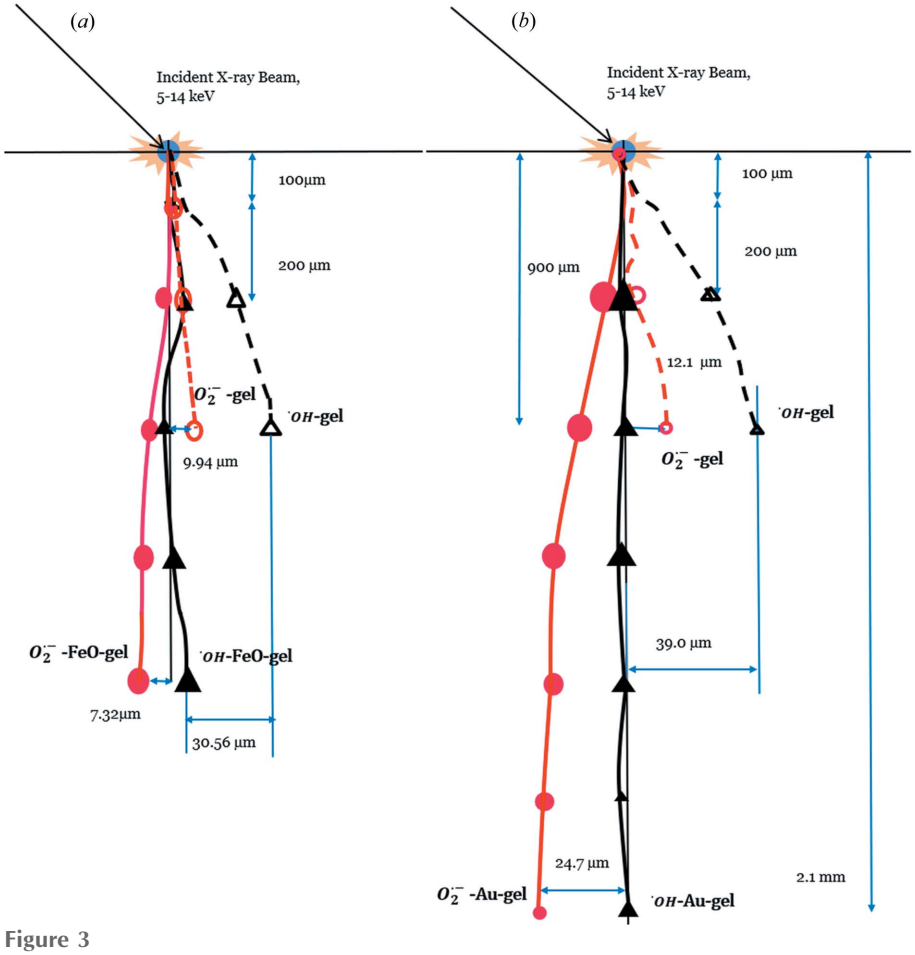

Figure 3
Nanoradiator X-FL-derived ROS distribution from either X-ray or electron emission in the depth direction of the ROS gel from the site of generation inside the cell, detected in (*a*) the AuNP-ROS gel and (*b*) the FeONP-ROS gel under X-ray irradiation in the absence or presence of nanoparticles. The Au-nanoradiator showed a longer penetration track and wider angular deflection than the Fe-nanoradiator along the depth direction.

The horizontal ROS distribution in a given depth is plotted along the penetration depth in Figs. 4 and 5. The fluorescent area from Au-nanoradiator-derived $^{\bullet}OH$ radicals diminished gradually as the X-FL penetrated further, while the Fe-nanoradiator-derived $^{\bullet}OH$ spread over increasingly larger areas. At a given depth, the $^{\bullet}OH$-fluorescence area derived from the Au-nanoradiator was smaller than the Fe-nanoradiator-derived $^{\bullet}OH$ fluorescence, in contrast to the similar scale of the $O_2^{\bullet-}$ fluorescence area for both the Au- and Fe-nanoradiators. This behavior may represent a difference in the LET of X-FL from Fe- and Au-nanoradiators, which may result in wider cellular damage from Fe-nanoradiator-derived $^{\bullet}OH$ than from Au-nanoradiator-derived OH at a given depth. Moreover, the fluorescence intensity ratio of $^{\bullet}OH$-APF to $O_2^{\bullet-}$-DHE was 1.36 ± 0.12 for the Au-nanoradiator and 3.22 ± 0.23 for the Fe-nanoradiator. These differences in the relative yields of $^{\bullet}OH$ FL and $O_2^{\bullet-}$ suggested relatively higher electron emission from the Au-nanoradiator than from the Fe-

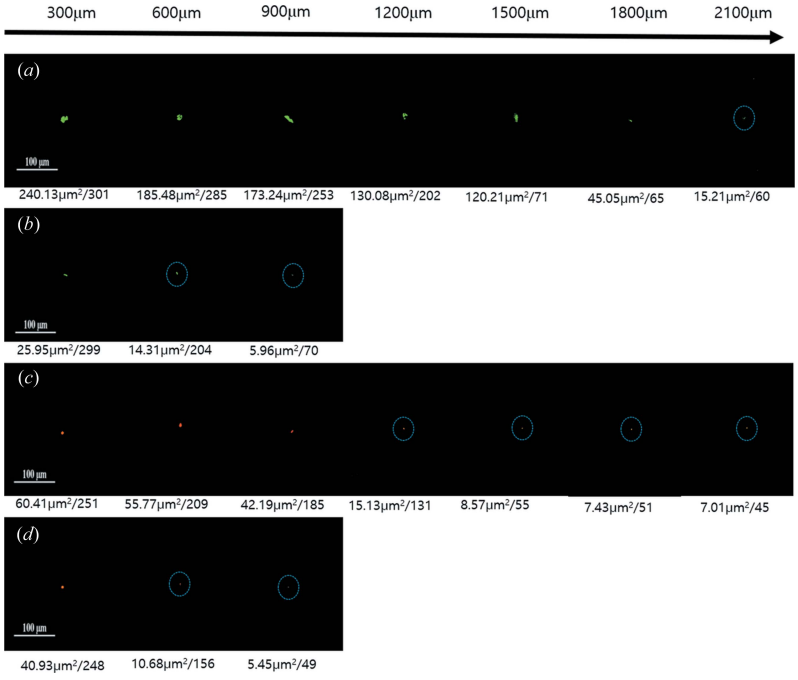

Figure 4
Au X-FL-derived planar ROS distribution detected by APF gel [green fluorescence (*a*) and (*b*)] or DHE gel [red fluorescence (*c*) and (*d*)] under X-ray irradiation in the absence (*b* and *d*) or presence (*a* and *c*) of AuNPs. The measured intensity and area of each ROS fluorescence are displayed, and in both cases the OH-radical fluorescence showed a gradual decrease with depth.

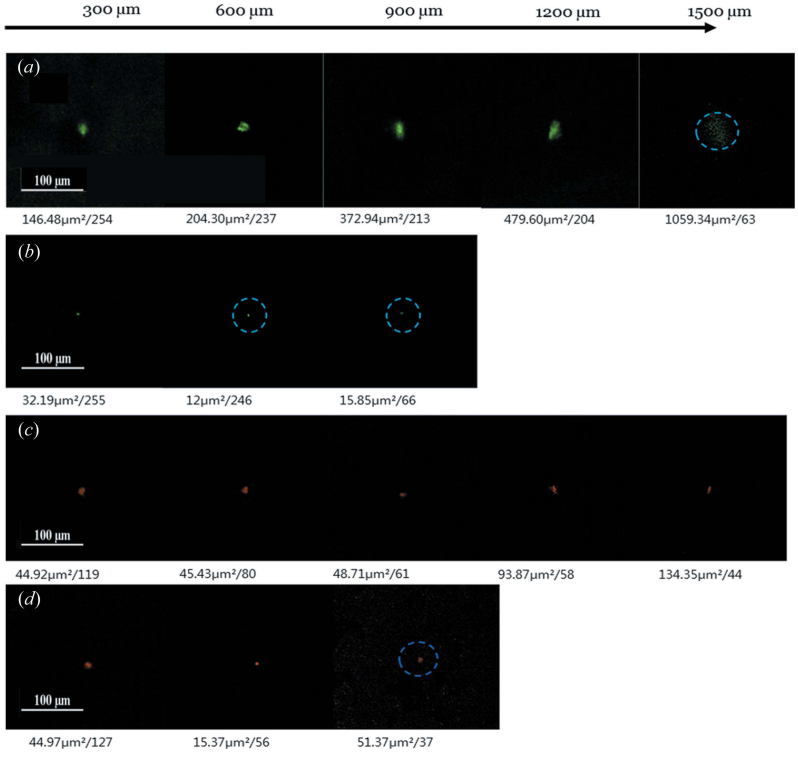

Figure 5
Fe X-FL-derived planar ROS distribution detected by APF gel [green fluorescence (*a*) and (*b*)] or DHE gel [red fluorescence (*c*) and (*d*)] under X-ray irradiation in the absence (*b* and *d*) or presence (*a* and *c*) of FeONPs. The measured intensity and area of each ROS fluorescence are displayed, and the OH radicals show a gradual decrease in intensity and increase in area with depth.

nanoradiator. The higher yield of electrons from the Au-nanoradiator is caused by the higher *Z*-number of gold, which effectively results in more electrons emitted from Auger cascades and intermolecular/interatomic Coulombic decay (Gokhberg *et al.*, 2014; Seo *et al.*, 2015), as has been demonstrated theoretically (Pradhan *et al.*, 2009). These differences were experimentally observed by ROS measurements under either proton (Seo *et al.*, 2017) or X-ray irradiation (Misawa & Takahashi, 2011).

4. Conclusions

A method that combines the use of 3D ROS gel and confocal laser-scanning fluorescence microscopy enables a new dosimetry-based track analysis of the radiation emitted by a nanoradiator. This method was demonstrated here by using a nanoparticle-containing single cell that had been selectively irradiated with an X-ray microbeam and analyzed by micrometre-scale laser scanning. The ROS-oxidant fluorescence, due to the nanoradiators, showed greater electron-mediated dose enhancement as well as deeper penetration for Au-nanoradiators than for Fe-nanoradiators. The ROS-composition and depth profile analyses of the nanoradiator dose suggested a role of the nanoradiator effect as an internal emitter and different extents of potential cellular damage for gold and iron oxide nanoparticles.

Funding information

This work was carried out with financial support from the National Research Foundation of Korea, funded by the Ministry of Education, Science and Technology (Grant Nos. 2013M2B2B1075774 and 2015M2A2A7A1045270).

References

Carter, J. D., Cheng, N. N., Qu, Y., Suarez, G. D. & Guo, T. (2007). *J. Phys. Chem. B*, **111**, 11622–11625.
Cho, E. C., Au, L., Zhang, Q. & Xia, Y. (2010). *Small*, **6**, 517–522.
Choi, G.-H., Seo, S.-J., Kim, K.-H., Kim, H.-T., Park, S.-H., Lim, J.-H. & Kim, J.-K. (2012). *Radiat. Oncol.* **7**, 184–194.
Gokhberg, K., Kolorenč, P., Kuleff, A. I. & Cederbaum, L. S. (2014). *Nature (London)*, **505**, 661–663.
Hainfeld, J. F., Dilmanian, F. A., Slatkin, D. N. & Smilowitz, H. M. (2008). *J. Pharm. Pharmacol.* **60**, 977–985.
Haume, K., Rosa, S., Grellet, S., Śmiałek, M. A., Butterworth, K. T., Solov'yov, A. V., Prise, K. M., Golding, J. & Mason, N. J. (2016). *Cancer Nanotechnol.* **7**, 8.

Jeon, J.-K., Han, S.-M. & Kim, J.-K. (2016*b*). *J. Synchrotron Rad.* **23**, 1191–1196.
Jeon, J.-K., Han, S.-M., Min, S.-K., Seo, S.-J., Ihm, K., Chang, W.-S. & Kim, J.-K. (2016*a*). *Sci. Rep.* **6**, 37848.
Kim, J.-K., Seo, S.-J., Kim, H.-T., Kim, K.-H., Chung, M.-H., Kim, K.-R. & Ye, S.-J. (2012). *Phys. Med. Biol.* **57**, 8309–8323.
Kim, J.-K., Seo, S.-J., Kim, K.-H., Kim, T.-J., Chung, M.-H., Kim, K.-R. & Yang, T.-K. (2010). *Nanotechnology*, **21**, 425102.
Lechtman, E., Chattopadhyay, N., Cai, Z., Mashouf, S., Reilly, R. & Pignol, J. P. (2011). *Phys. Med. Biol.* **56**, 4631–4647.
Leung, M. K. K., Chow, J. C. L., Chithrani, B. D., Lee, M. J. G., Oms, B. & Jaffray, D. A. (2011). *Med. Phys.* **38**, 624–631.
Misawa, M. & Takahashi, J. (2011). *Nanomed. Nanotechnol. Biol. Med.* **7**, 604–614.
Nambara, K., Niikura, K., Mitomo, H., Ninomiya, T., Takeuchi, C., Wei, J., Matsuo, Y. & Ijiro, K. (2016). *Langmuir*, **32**, 12559–12567.
Penn, C. A., Yang, K., Zong, H., Lim, J.-Y., Cole, A., Yang, D., Baker, J., Goonewardena, S. N. & Buckanovich, R. J. (2018). *Small Mol. Therapeut.* **17**, 96–106.
Porcel, E., Tillement, O., Lux, F., Mowat, P., Usami, N., Kobayashi, K., Furusawa, Y., Le Sech, C., Li, S. & Lacombe, S. (2014). *Nanomed. Nanotechnol. Biol. Med.* **10**, 1601–1608.
Pradhan, A. K., Nahar, S. N., Montenegro, M., Yu, Y., Zhang, H. L., Sur, C., Mrozik, M. & Pitzer, R. M. (2009). *J. Phys. Chem. A*, **113**, 12356–12363.
Rothen-Rutishauser, B., Kuhn, D. A., Ali, Z., Gasser, M., Parak, W. J., Vanhecke, D., Fink, A., Gehr, P. & Brandenberger, C. (2013). *Nanomedicine*, **9**, 607–621.
Schuemann, J., Berbeco, R., Chithrani, B. D., Cho, S., Kumar, R., McMahon, S., Sridhar, S. & Krishnan, S. (2016). *Int. J. Radiat. Oncol. Biol. Phys.* **94**, 189–205.
Seo, S.-J., Han, S.-M., Cho, J.-H., Hyodo, K., Zaboronok, A., You, H., Peach, K., Hill, M. A. & Kim, J.-K. (2015). *Radiat. Environ. Biophys.* **54**, 423–431.
Seo, S.-J., Jeon, J.-K., Han, S.-M. & Kim, J.-K. (2017). *Int. J. Radiat. Biol.* **93**, 1239–1247.
Vinogradov, S., Warren, G. & Wei, X. (2014). *Nanomedicine*, **9**, 695–707.
Wolfe, T., Chatterjee, D., Lee, J., Grant, J. D., Bhattarai, S., Tailor, R., Goodrich, G., Nicolucci, P. & Krishnan, S. (2015). *Nanomedicine*, **11**, 1277–1283.
Xie, X., Liao, J., Shao, X., Li, Q. & Lin, Y. (2017). *Sci. Rep.* **7**, 3827.
Yang, C., Bromma, K., Ciano-Oliveira, C. D., Zafarana, G., van Prooijen, M. & Chithrani, D. B. (2018). *Cancer Nanotech.* **9**, 4.